Lubricant Flow and Evaporation Model for Heat Assisted Magnetic Recording Including Functional End-Group Effects and Thin Film Viscosity

Joanna Bechtel Dahl

David B. Bogy

April 4, 2013

Abstract

The lubricant covering a hard disk in a heat assisted magnetic recording drive must be able to withstand the writing process in which the disk is heated several hundred degrees Celsius within a few nanoseconds to reduce the coercivity of the media and allow writing of data. As a first step in developing and modeling a robust lubricant, we model and predict the flow and evaporation of a conventional perfluoropolyether lubricant, Zdol 2000, for which there exists experimental data. We have developed a simulation tool that, for the first time, incorporates into a continuum model the film thickness dependencies of viscosity and extra contributions to disjoining pressure due to functional end-groups. Simulations at small length and time scales that are unobservable with current experimental capabilities are performed. We investigate the effect of the total disjoining pressure and thin film viscosity on evaporation and lubricant flow for different initial thickness. For films thicker than 1 nm, the inclusion of polar disjoining pressure suppresses the lubricant thickness change due to evaporation and thermocapillary shear stress compared with cases without this component. Thin film viscosity is important to consider for thinner lubricants. We also consider how lubricant depletion changes with laser spot size and thermal spot maximum temperature. The smaller spot profiles have side ridges due to thermocapillary shear stress while the larger spot profiles show no side ridges, only a trough due to evaporation. The lubricant depletion zone width and depth increase with increasing thermal spot maximum temperature.

1 Introduction

The magnetic recording industry widely views heat assisted magnetic recording (HAMR) as a technology to achieve storage densities beyond 1 Tb/in^2 in hard disk drives [1, 2, 3]. Novel components such as a laser delivery system integrated into the slider and a new

magnetic medium have been developed to the point that a recent spin-stand recording demonstration of HAMR system technology claims to have achieved 1.007 Tb/in^2 [4]. Continued developments in the tribological design of the head-disk interface (HDI) is required along with advancements of other HAMR system components in order to maintain the mechanical reliability of the head/disk interface despite decreased spacing and adverse thermal conditions. One critical component of the HDI is the lubricant coating on the magnetic disk that protects the disk and recording head from damage due to intermittent contacts during normal drive operations when the recording head is flying over the spinning disk with a minimum clearance ~ 5 nm and relative velocity around 10 m/s. The HAMR lubricant must be able to withstand the writing process in which the disk is locally heated a few hundred degrees Celsius within a few nanoseconds to reduce the coercivity of the media and allow writing of data.

Perfluoropolyethers (PFPEs) are common lubricants used in the magnetic recording industry due to their favorable properties that enable them to reduce wear and friction at conventional hard drive operating temperatures throughout the drive lifetime: chemical stability, low volatility, thermal stability, and low viscosity. Lubricant properties can be further improved and customized by adding functional end-groups, such as the hydroxyl end-groups of Fomblin Zdol that interact with the amorphous carbon overcoat through hydrogen bonding [5]. The chemical structure of the common Fomblin Zdol lubricant is

$$\mathrm{HO-CH_2CF_2-(OCF_2CF_2)_n-(OCF_2)_m-O-CF_2CH_2-OH}$$

where the ratio m/n is typically between 2/3 and 1. This polymer chain is composed of a perfluorinated ether backbone terminated by hydroxyl groups. The HAMR writing system will create an adverse thermal environment for PFPE lubricants as the magnetic media is heated above its Curie temperature around 402–477°C with large temperature gradients due to the estimated small spot size of only 25 nm full width half maximum (FWHM) to achieve 5 Tb/in^2 [3]. Thermal decomposition of bulk Fomblin Zdol occurs at temperature above 350°C [6, 7] and evaporation of functionalized PFPEs will be significant at HAMR system temperatures [8, 9], so a new HAMR lubricant needs to be designed to achieve HDI reliability. As a first step in developing and modeling a robust lubricant, we model and predict the flow and evaporation of conventional Zdol lubricants, for which there exists experimental data.

Several experimental studies have investigated depletion mechanisms of conventional lubricants, usually Zdol, due to localized heating during the HAMR writing process. The Tagawa group at Kansai University have developed a spinstand unit to test lubricant-coated hard disks subject to laser irradiation from an optically focused laser incident with a large spot diameter of 900 nm. In these studies in which a slider was not flying over the disk and the maximum temperature achieved in most experiments was less than 100°C, the effects of lubricant thickness, bonding ratio, molecular weight, end-group, and laser power have been investigated [10, 11, 12, 13]. Experimentalists at the Data Storage Institute have also developed a HAMR tester, which includes an optically focused 0.9–1 μm laser spot heating the disk to an estimated maximum temperature as high as 360°C; however the laser had to be scanned back and forth to create irradiation tracks 10–20 μm wide in order for the lubricant depletion to be visible on the optical surface analyzer [14, 15, 16, 17].

Lubricant flow and evaporation under HAMR writing conditions has been studied numerically as well. Wu developed a continuum-based lubricant flow model under a scanning laser (laser intensity profile assumed Gaussian with standard deviation 33.33 nm) and found that evaporation removes a majority of lubricant from the disk surface when it is heated to 301°C within 20 ns while thermocapillary shear stress and thermoviscosity have a smaller effect [18]. Wu and Talke improved upon this model by solving the Fourier heat conduction problem in a multi-layered HAMR disk to determine the disk surface temperature driving the lubricant flow [19]. Similar HAMR lubricant simulations were conducted in [20], and the authors investigated the effects of evaporation enthalpy, initial film thickness, and evaporation coefficient on lubricant depletion due to a Gaussian profile laser beam with standard deviation 33.33 nm and maximum disk surface temperature calculated to be 281°C . Matsuoka et al. [21] analyzed lubricant deformation considering a temperature and film thickness dependence of surface tension they derived from integration of a corrected van der Waals pressure equation, subjecting the lubricant to a Gaussian temperature profile with standard deviation 1 μm and maximum temperature rise of 100°C . Most lubricant simulation results in the literature have included only the component of disjoining pressure due to long-range van der Waals interactions with a form $1/h^3$, or in the case of [21] surface tension enhanced by van der Waals forces of the form $1/h^2$, and therefore simulate non-functional lubricants. Zhou et al. [22] did include a polar disjoining pressure component, but their simulation results investigated only evaporation rate and not lubricant flow on the disk. Lubricants with functional end-groups are likely to be used, so disjoining pressure that includes more than van der Waals interactions should be considered in HAMR lubricant modeling. The strong interactions between the functional end-groups and the disk substrate will also create a restricted layer having an effective viscosity much larger than the mobile layers above or the bulk lubricant [23].

In this report we develop a simulation tool that incorporates film thickness dependencies of viscosity and extra contributions to disjoining pressure due to functional end-groups into a continuum lubrication model for lubricant flow on the HAMR disk surface. Simulations are carried out for length and time scales unobservable with current experimental capabilities–illumination times of a couple nanoseconds and laser spot sizes less than 100 nm. We investigate the effect of the total disjoining pressure and thin film viscosity on evaporation and lubricant flow for different initial thickness. We also consider how lubricant depletion changes with laser spot size and thermal spot maximum temperature.

2 Lubricant Model

2.1 Governing Evolution Equation

Lubrication theory based on continuum mechanics exploits the difference in length scales between the film thickness direction and the planar directions. In our case, the characteristic film thickness h_0 is close to 1 nm. This is much smaller than the characteristic slider ($\sim$ 800 μm) and at least an order of magnitude smaller than the expected laser FWHM used in HAMR ($\sim$ 25 nm for ultra high density HAMR recording of 5

Tb/in^2 [3]). Thus the key requirement of lubrication theory is satisfied in our system.

We are obviously pushing the limits of continuum theory by using lubrication theory to describe the HAMR lubricant. The PFPE backbone of molecular weight 2 kg/mol (Zdol 2000) has a radius of gyration of 1.2 nm in Freon [24], meaning a 1 nm thick PFPE film is one or two monolayers and the discrete nature of individual molecules may be important. However, other researchers have found that continuum theory can be an adequate approach for predicting PFPE lubricant flow on a hard drive disk. Scarpulla et al. [23] found that thin film PFPE movement under air shearing is generally well described by a continuum flow process with an effective viscosity, even when the film thickness is less than the polymer's diameter of gyration. More recently, Marchon and Saito [25] found that under HAMR laser illumination conditions, continuum fluid dynamics simulations with a temperature dependent Hamaker constant agreed well with much more computationally expensive molecular dynamics simulations. Thus we will use the lubricant theory approach as a starting point for studying lubricant flow and evaporation under HAMR writing conditions.

In our application of the lubrication approximation, shown in Figure 1, the viscous liquid is bounded below by a horizontal solid substrate (the magnetic recording disk) and above by an interface between the liquid film and a passive gas (the air bearing). In this problem, the lubricant film thickness $h(x,y,t)$ is unknown and the unknown lubricant pressure $p(x,y,t)$ is a functional of h via the surface tension and disjoining pressure, as explained in Sections 2.2 and 2.3. PFPE lubricants exhibit viscoelastic behavior [24], but here we retain the purely viscous model. The incorporation of a viscoelastic constitutive model into our HAMR lubricant flow and evaporation simulations will be the subject of a future report.

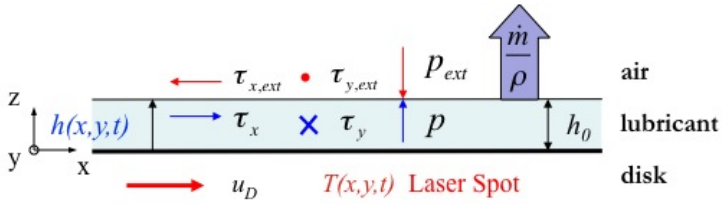

Figure 1: HAMR lubricant write process schematic: The thin lubricant film of unknown thickness $h(x,y,t)$ is subject to a scanning laser spot of speed u_D, which is represented by a prescribed Gaussian temperature distribution $T(x,y,t)$. Lubricant flow is driven by the resulting external shear stresses $\tau_{x,ext}$ and $\tau_{y,ext}$ and pressure gradient ∇p_{ext}. Some lubricant is removed from the film via evaporation ($\dot{m}$).

The final governing evolution equation for our HAMR lubricant system is:

$$\frac{\partial h}{\partial t} + u_D \frac{\partial h}{\partial x} + \frac{\partial}{\partial x}\left(-\frac{h^3}{3\eta}\frac{\partial p}{\partial x} + \frac{h^2}{2\eta}\tau_x\right) + \\ + \frac{\partial}{\partial y}\left(-\frac{h^3}{3\eta}\frac{\partial p}{\partial y} + \frac{h^2}{2\eta}\tau_y\right) + \frac{\dot{m}}{\rho} = 0 \qquad (1)$$

h is the unknown lubricant thickness, u_D is the disk velocity in the x direction corresponding to the down-track direction, η is the lubricant viscosity, p is the lubricant pressure, τ_x is the lubricant shear stress in the x direction (down-track), τ_y is the lubricant shear stress in the y direction (cross-track), ρ is the constant lubricant density, and $\dot{m}$ is the mass flux due to evaporation. A rigorous derivation of this governing evolution equation is presented in [26]. The lubricant pressure and shear stress are determined by a force balance at the lubricant-air interface. The following sections include a physical explanation of the intermolecular forces and lubricant property models that determine the interfacial forces and the final form of the governing equation.

Lubricant Properties and Interfacial Forces Intermolecular interactions between various components of the thin film system dictate the movement of the lubricant that covers the disk: lubricant-lubricant molecule interactions, lubricant-carbon overcoat interactions, and the presence of two interfaces in close proximity (air-lubricant and lubricant-carbon overcoat). In order to model the lubricant from a continuum point of view, we endow the lubricant with various macroscopic properties that capture the long-range effects of the intermolecular interactions on lubricant flow and evaporation. These properties are surface tension, disjoining pressure, viscosity, and vapor pressure. Vapor pressure determines the evaporation rate of the lubricant. Surface tension and disjoining pressure, in effect, apply forces to the lubricant-air interface and determine the lubricant pressure. In addition, we make an assumption about the density of the 1–2 nm lubricant film covering the disk.

2.2 Surface Tension

When the molecule is brought to the interface between the liquid and a gas, the molecule experiences intermolecular attractions from one side only. The unbalanced intermolecular forces near an interface means the interface has a thermodynamic surface energy γ_{LV} per unit area of liquid-vapor interface; in order to bring more molecules to the surface and increase the area of the interface, an additional energy γ_{LV} per unit of added area needs to be applied to the system [27, 28]. For liquids, surface energy can be interpreted as a force per unit length that acts tangent to the interface, and this force is commonly called surface tension: $\gamma = \gamma_{LV}$.

The resultant force of surface tension can be decomposed into two parts: a component tangent to the interface that is due to variations in surface tension (Maragoni stress) and a component acting normal to the interface due to surface curvature (Laplace pressure or capillary pressure) [29]. In this study the variation in surface tension is due to a temperature gradient, and the resulting Maragoni stress is also called thermocapillary stress. Thus surface tension contributes to the force balance at the lubricant air interface via its resultant applied pressure and shear stress:

$$\begin{aligned} p_{ext}\mathbf{n}\Big|_{\gamma} &= (-\gamma\nabla\cdot\mathbf{n})\,\mathbf{n} = \left(\gamma\nabla^2 h\right)\mathbf{n} \\ \tau_{ext}\Big|_{\gamma} &= \nabla\gamma - \mathbf{n}\,(\nabla\gamma\cdot\mathbf{n}) \end{aligned}$$

where $\mathbf{n}$ is the interface unit normal vector and the gradient is a two-dimensional operator: $\nabla(\cdot) = \frac{\partial}{\partial x}(\cdot)\mathbf{e}_1 + \frac{\partial}{\partial y}(\cdot)\mathbf{e}_2$. For quasi-parallel films ($|\nabla h| \ll 1$), $\mathbf{n} \approx \mathbf{e}_3$, so $\nabla\gamma \cdot \mathbf{n} \approx 0$. Therefore the external forces on the lubricant-air interface due to surface tension are

$$p_{ext}\mathbf{n}\Big|_\gamma = \left(\gamma\nabla^2 h\right)\mathbf{e}_3 \tag{2}$$

$$\tau_{ext}\Big|_\gamma = \frac{\partial\gamma}{\partial x}\mathbf{e}_1 + \frac{\partial\gamma}{\partial y}\mathbf{e}_2 \tag{3}$$

The surface tension of most liquids decreases with increasing temperature until it reaches a value of zero at the critical temperature. The surface tension of a nonpolar PFPE lubricant was measured in the limited temperature range of 10-180°C and found to be linear [21]. We assume that functional PFPE lubricants such as Zdol have a similar slope, and in our model we will use the slope $\frac{d\gamma}{dT} = -0.06$ mN/(m°C). With this assumed dependence on temperature, the external shear stress due to surface tension (thermocapillary shear stress) becomes

$$\tau_{ext}\Big|_\gamma = \frac{d\gamma}{dT}\frac{\partial T}{\partial x}\mathbf{e}_1 + \frac{d\gamma}{dT}\frac{\partial T}{\partial y}\mathbf{e}_2 \tag{4}$$

where T is the local lubricant temperature. For the simulations in this report, $T(x,y)$ is prescribed so the temperature gradient is a known quantity.

2.3 Disjoining Pressure

For sufficiently thin films, the lubricant molecules at the lubricant-air interface experience intermolecular forces from liquid molecules in the film and molecules in the solid substrate. In effect, these intermolecular forces have a finite range r, as schematically illustrated in Figure 2. First introduced by Derjaguin, disjoining pressure is defined as the difference between the hydrostatic pressure p in the thin liquid film and the pressure of the bulk phase p_∞ under the same thermodynamic conditions (equal temperature and chemical potential) [30]:

$$\Pi(h) = p - p_\infty$$

This additional or supplementary pressure acting on a interfacial surface element produces an extra force that augments the classical equations of hydrostatics. This new force in thin film systems is a function of film thickness only, and it is proportional to surface area. It is the resultant force of all intermolecular interactions within the solid-liquid-vapor system exerted by the solid on the interfacial surface element dA. Disjoining pressure can be positive (solid substrate repels interface) or negative (solid substrate attracts interface). Thus the contribution of disjoining pressure acting on interfacial elements is

$$p_{ext}\mathbf{n}\Big|_\Pi = \Pi(h)\mathbf{e}_3 \tag{5}$$

The challenge for accurately predicting lubricant behavior in hard disk drives has been to determine an appropriate model for the disjoining pressure of the particular lubricant-disk system of interest. We will consider two contributions to disjoining pressure and use the mischaracterizing terminology common in hard drive lubricant

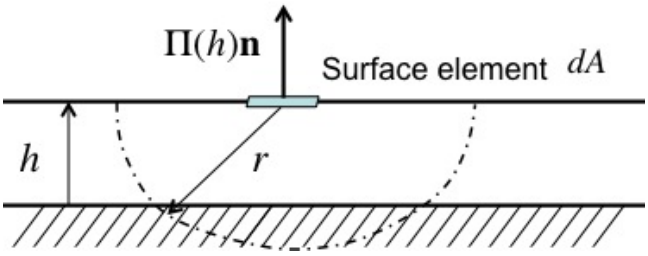

Figure 2: Disjoining pressure is the resultant force of intermolecular interactions in the solid-liquid-vapor system within a range of influence r on the interfacial surface element dA.

literature [31]: (1) the *dispersive component* due to van der Waals forces with $1/h^3$ dependence and (2) the oscillating *polar component* that could be due to structural effects or non van der Waals interactions introduced by the functional end-groups. Previous simulations for lubricants covering the disk under HAMR conditions have only considered the dispersive component.

The sessile drop method to determine disjoining pressure of hard drive lubricants from experimental surface energy (contact angle) data has been widely used. However, some researchers have questioned the assumptions made in this method and caution that while such experiments and analysis are useful probes for determining lubricant-substrate dynamics, the values determined for disjoining pressure should not be taken as a true experimental measurement [31, 33]. In the absence of an accurate method to measure disjoining pressure, we use the mathematical model for PFPE Zdol from Karis and Tyndall [32] derived using (suspicious) contact angle measurements from their earlier publications [34, 35, 36]. The authors assumed a $1/h^2$ form of the dispersive component of surface free energy consistent with the $1/h^3$ form for dispersive disjoining pressure and determined the coefficients by a regression fit to their earlier dispersive surface energy data: $\gamma^d = c_0 + c_1/h^2$. Using the notation from [32], here γ is surface energy. The oscillating polar component of surface energy is fit to the polynomial expansion $\gamma^p = \sum_{i=0}^{n} a_i h^i$. The disjoining pressure is the negative derivative of the the free energy gradient with respect to:

$$\Pi = -\frac{d\gamma}{dh} = -\frac{d\gamma^d}{dh} - \frac{d\gamma^p}{dh} = \Pi^d + \Pi^p$$

The disjoining pressure and its derivative for Zdol from [32] are plotted against film thickness in Figure 3. Note that surface energy measurements can vary significantly with lubricant end-group, molecular weight, and production processes such as annealing [34], so by employing this model, we are confining our simulation results to predict the behavior of the lubricant-disk systems used in the experimental data to which the disjoining pressure model was fit (unannealed Zdol 2000 coating a production magnetic disk with a 1.3 nm thick amorphous hydrogenated carbon overcoat). We are also limiting our simulations to 0.2 - 2 nm because that is the limit of the experimental data

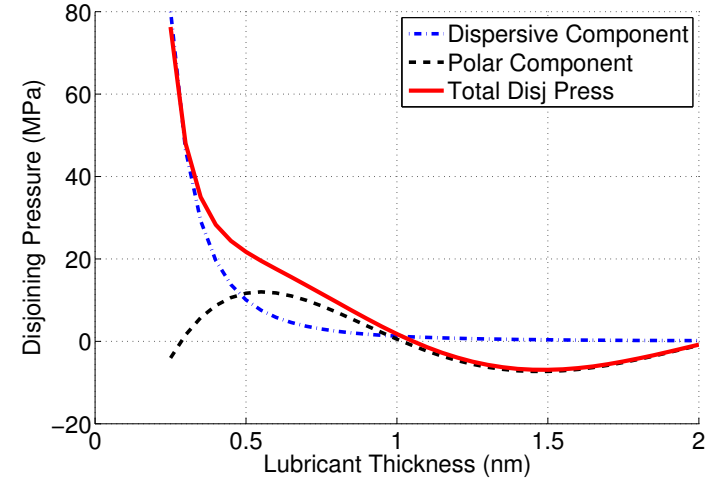

(a) Disjoining pressure $\Pi(h)$

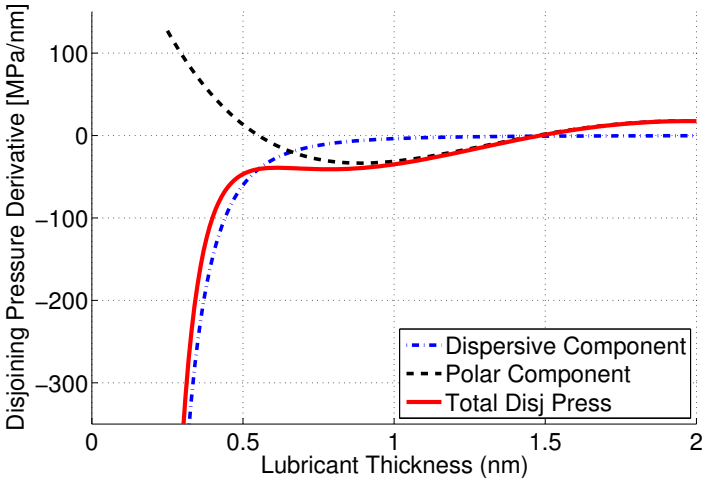

(b) Disjoining pressure derivative $\frac{d\Pi}{dh}$

Figure 3: Disjoining pressure model from [32]. This model is derived from experimental free energy measurements (sessile drop method) of unannealed PFPE Zdol 2000 on magnetic disks with a 1.3 nm amorphous hydrogenated carbon overcoat.

on which the disjoining pressure model is based. Other kinds of lubricants will have different intermolecular interactions and therefore need a different disjoining pressure model.

2.4 Viscosity

An explicit formula for viscosity can be derived by applying the method of absolute reaction rates to pure liquids. In this approach, credited to Eyring [37], viscosity and diffusion in a liquid are viewed as rate processes, similar to chemical kinetics. In Eyring's model, flow occurs when one molecule squeezes past its neighbors, passing through a "flow-activated state" in which intermolecular potential energies are high due to closer proximity with neighboring molecules, and drops into a vacant equilibrium position. Eyring reasoned that because some of the same intermolecular bonds are broken in a flow process as in a vaporization process, the activation energies of viscous flow can be estimated from vaporization energies.

Karis [38] applied Eyring's rate theory to hard disk drive lubricants. The resulting thin film viscosity model is

$$\eta = \left(\frac{N_A h_P}{V_l}\right) \exp\left(\frac{\Delta E_{vis} - T\Delta S_{vis}}{RT}\right) \tag{6}$$

N_A is Avogadro's number, h_P is Plank's constant, V_l is the molar volume (moles per unit volume) of the lubricant, R is the universal gas constant, and T is the system temperature. ΔE_{vis} and ΔS_{vis} are the flow-activation energy and entropy that depend on film thickness. We use the same reasoning and ΔE_{vis} and ΔS_{vis} values found in [38] for Zdol.

In contrast to the work we present in this report, earlier simulations of hard drive lubricants under HAMR conditions have included only the temperature dependence on viscosity [18, 19, 20]. This chemical kinetics model for viscosity gives the same trend with temperature but also includes the effects of a thinning film of lubricant flow.

2.5 Vapor Pressure and Evaporation Rate

Vapor pressure depends on the system temperature and the nature and strength of the intermolecular interactions that need to be overcome for a molecule to escape the condensed state and vaporize. For PFPE lubricants, longer molecular chains (higher molecular weight) mean more interactions to overcome during vaporization; therefore, higher molecular weight lubricants have a lower vapor pressure. We use the method of Karis [24] to calculate the bulk vapor pressure $p_{vap,\infty}(T, M_w)$ of Zdol with the Clapeyron equation and employing the ideal gas law. The linear relationship between vaporization activation energy and molecular weight for Zdol was determined by comparing simulated evaporation data with that measured by isothermal thermogravimetric analysis [9].

Independent of its origin, a pressure difference across an interface causes a change in the equilibrium vapor pressure from the bulk value at a given temperature [39]. The long-range intermolecular interactions between the liquid film molecules and the solid substrate that give rise to disjoining pressure and the curvature of the interface modify the vapor pressure of the thin film lubricant system by adding to the system's chemical potential. Expressions for the liquid and vapor phase chemical potentials are found by integrating the the Gibbs-Duhem equation, and the final result of equilibrium thin film

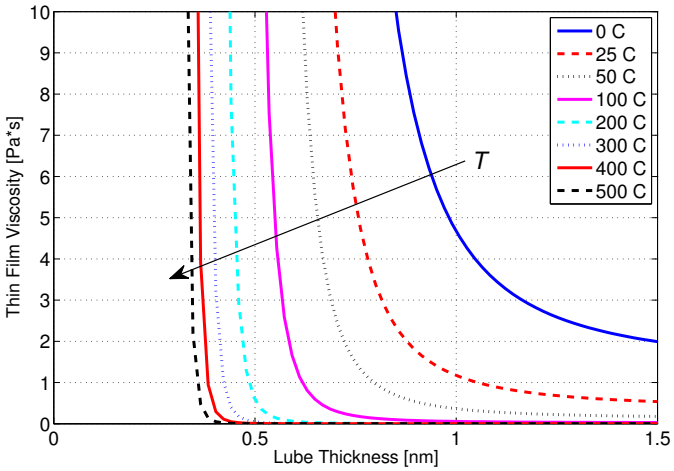

Figure 4: Viscosity model for PFPE Zdol from [38] based on Eyring's rate theory [37]. The arrow points in direction of increasing temperature.

vapor pressure for a given system temperature T is determined by equating the liquid and vapor chemical potentials [40]:

$$\frac{p_{vap,film}}{p_{vap,\infty}} = \exp\left(\frac{M_w}{\rho RT}\left[-\Pi(h) - \gamma\nabla^2 h\right]\right) \tag{7}$$

We assume a simple constitutive model for the rate of evaporation of the lubricant based on kinetic theory (collision theory). The Hertz-Knudsen-Langmuir model for evaporation/condensation specifies that the evaporation or condensation rate is proportional to the difference between the equilibrium vapor pressure and the current vapor pressure [41]:

$$\dot{m} = \alpha\frac{M_w}{\sqrt{2\pi RT}}\left(p_{vap} - p_i\right) \tag{8}$$

$\dot{m}$ is the evaporative mass flux (units mass/time per unit area), M_w is the molecular weight of the liquid molecules (mass per mole), R is the molar universal gas constant, and T is the liquid-vapor system common temperature. α is a evaporation coefficient (sometimes called the accommodation coefficient) that accounts for imperfect evaporation and the shortcomings of collision theory to describe real systems. p_{vap} is the equilibrium vapor pressure and p_i is the current vapor pressure, i.e. the partial pressure of the adjacent vapor in the gas mixture (evaporated liquid vapor plus an inert component). This simple model says there will be a net evaporation rate as long as the partial pressure of the evaporated substance immediately above the interface is less than the vapor pressure ($p_i < p_{vap}$).

Furthermore, we simplify the evaporation model by making additional assumptions. Recently, researchers have matched this evaporation model to relatively low

temperature ($< 240^{\circ}$C) experimental data and claim that the accommodation coefficient is approximately 1 for $T < 133^{\circ}$C and decreases exponentially with increasing temperature up to the limit of experiments [42]. As evaporation accommodation is not the focus of this study and adds further complication, for our simulations we will assume $\alpha = 1$, thereby giving a high prediction of the amount of evaporation. In addition, we assume that the lubricant is being evaporated into rarefied air that has no lubricant molecules in a vapor state ($p_i = 0$). We consider this a reasonable assumption when the disk linear velocity is around 10 m/s, thereby quickly shearing away recently evaporated lubricant. Our final evaporation model is:

$$\dot{m}(T, M_w, h) = \frac{M_w}{\sqrt{2\pi RT}} p_{vap,\infty} \exp\left(\frac{M_w}{\rho RT}\left[-\Pi - \gamma\nabla^2 h\right]\right) \tag{9}$$

2.6 Density

Density appears in the governing equation evaporation source term. Variation of density in thin liquid PFPE films on solid substrates has been studied numerically with Monte Carlo simulations [43]. The authors found that the density of the polymer decreases near the surface, and they suggested this decrease in density is due to resistance to the diffusion of polymers by the impenetrable surface. According to the plots in [43], the density of thin films less than 2 nm is about 10% less than the two sublayers above. So we approximate the thin film density in our simulations of systems < 2 nm as 10% less than the bulk value Zdol 2000 density value given in the Fomblin Z Derivatives Data Sheet: $\rho = 1630$ kg/m^3.

2.7 Non-dimensionalized Lubricant System

Substituting in the determined lubricant pressure and shear stresses and designating $c = -\frac{d\gamma}{dT} > 0$, the dimensional governing equation is

$$\begin{aligned}\frac{\partial h}{\partial t} + u_D \frac{\partial h}{\partial x} + \frac{\partial}{\partial x}\left[\frac{h^3}{3\eta}\frac{\partial}{\partial x}\left(\Pi + \gamma\nabla^2 h\right) - \frac{h^2}{2\eta} c \frac{\partial T}{\partial x}\right] + \\ \frac{\partial}{\partial y}\left[\frac{h^3}{3\eta}\frac{\partial}{\partial y}\left(\Pi + \gamma\nabla^2 h\right) - \frac{h^2}{2\eta} c \frac{\partial T}{\partial y}\right] + \frac{\dot{m}}{\rho} = 0\end{aligned} \tag{10}$$

We use a similar non-dimensionalization scheme as Wu [18]. The obvious non-dimensionalizations are based on system parameters of initial lubricant thickness h_0, prescribed temperature profile FWHM L, ambient temperature T_0, maximum prescribed temperature rise $\Delta T = T_{max} - T_0$, and initial ambient lubricant properties $\eta_0 = \eta(T_0, h_0)$ and $\gamma_0 = \gamma(T_0)$:

$$\begin{aligned} h_* &= h\,h_0 \qquad & x_* &= x\,L \qquad & y_* &= y\,L \\ \eta_* &= \eta\,\eta_0 \qquad & \gamma_* &= \gamma\,\gamma_0 \qquad & T_* &= T\,\Delta T + T_0 \end{aligned} \tag{11}$$

We now switch to the notation that quantities with the asterisk subscript are dimensional and the quantities without the asterisk subscript are non-dimensional. The temporal t_s and pressure p_s scales as well as the non-dimensional advection velocity C_u

and evaporation source term S are determined in the non-dimensionalization process so that all quantities in the governing equation are of order one and have no coefficient.

$$t_* = t\,t_s \qquad p_* = p\,p_s \quad \text{where } p_* = \Pi_* \text{ or } \gamma_* \nabla^2 h_* \tag{12}$$

Substituting Equations 11 and 12 into Equation 10 and multiplying by $\frac{2\eta_0 L^2}{h_0^2 c\Delta T}$ so that the thermocapillary shear stress terms have a coefficient of one, we determine that the scales and coefficients are as follows:

$$\begin{aligned} t_s &\equiv \frac{2\eta_0 L^2}{h_0 c\Delta T} \qquad & p_s &\equiv \frac{3}{2}\frac{c\Delta T}{h_0} \\ C_u &\equiv \frac{2\eta_0 L}{h_0 c\Delta T} u_D \qquad & S &\equiv \frac{2\eta_0 L^2}{h_0^2 c\Delta T}\frac{\dot{m}}{\rho} \end{aligned} \tag{13}$$

The final non-dimensional governing equation for the lubricant flow and evaporation simulations is:

$$\begin{aligned} \frac{\partial h}{\partial t} + C_u \frac{\partial h}{\partial x} + \frac{\partial}{\partial x}\left[\frac{h^3}{\eta}\frac{\partial}{\partial x}\left(p_{disj} + p_{Lap}\right) - \frac{h^2}{\eta}\frac{\partial T}{\partial x}\right] + \\ \frac{\partial}{\partial y}\left[\frac{h^3}{\eta}\frac{\partial}{\partial y}\left(p_{disj} + p_{Lap}\right) - \frac{h^2}{\eta}\frac{\partial T}{\partial y}\right] + S = 0 \end{aligned} \tag{14}$$

where $p_{disj} = \Pi / p_s$ and $p_{Lap} = \gamma \nabla^2 h / p_s$.

3 Numerical Scheme

The numerical scheme used to solve the non-linear governing equation 14 is based on the simulation code developed by H. Kubotera while he was a visiting scholar at the Computer Mechanics Laboratory [44]. Equation 14 is discretized using the control volume method [45]. First derivatives are approximated by the second-order accurate central difference scheme, and the second derivates in the Laplacian operator are approximated by a fourth-order accurate second derivative finite difference scheme. The code takes advantage of the symmetry in y (cross-track direction).

The governing hyperbolic equation is divided into its non-advective (Eulerian) and advective (Lagrangian) phases. First the non-advective part is iteratively solved with a Gaussian elimination scheme until the convergence criterion is met. Once the Eulerian phase is advanced, the advective phase is solved with the Cubic Interpolated Propagation (CIP) scheme [46, 47]. With no advection velocity in the y direction, our solution is one dimensional with regard to the advection scheme. A cubic interpolation function $F(x)$ between spatial grid points uses matching conditions of both the physical value $h(x,t)$ as well as it's first spatial derivative $\frac{\partial h}{\partial x}$, and this interpolant is used to advance $h(x,t)$ and $\frac{\partial h}{\partial x}$ from time point n to $n+1$.

At the edge of the computation domain, the temperature is ambient and the Dirichlet boundary conditions are $h = h_0$.

4 Simulations Under HAMR Write Conditions

In the HAMR writing process, a complicated laser delivery system will transfer enough energy to the magnetic layer to heat it above its Curie temperature so that the magnetic field generated by the magnetic write pole can flip the magnetic bits. We perform simulations that investigate how the lubricant flows and evaporates under write conditions due to the scanning thermal spot.

The transfer of optical energy from the laser diode, through the waveguide, to the near-field transducer where it is believed the optical energy is converted to electronic plasmons, and finally somehow conveyed through the nanometers-thick air bearing, lubricant, and overcoat to the magnetic layer is a complicated and not well understood nanoscale heat transfer problem. We avoid these complications by prescribing a Gaussian temperature profile on the rotating disk surface to approximate the final result of the HAMR laser delivery system. We assume the 1–2 nm lubricant layer has the same temperature as the disk surface because it is so thin. For all simulations that follow, the ambient conditions are $T_0 = 25°\mathrm{C}$ and $p_0 = 101325$ Pa = 1 atm. All simulations are for Zdol 2000, with a molecular weight 2 kg/mol.

In these simulation we do not include the air bearing pressure and shear stress or electrostatic pressure. Those effects are left to the subject of another lubricant study.

4.1 Driving Forces of Lubricant Distortion

The instigator of lubricant deformation under HAMR write conditions is the scanning thermal spot. Our model for the HAMR lubricant considers various lubricant properties that can depend on local temperature and lubricant deformation: surface tension, disjoining pressure, vapor pressure, and viscosity. Of these properties and their effects resulting from the applied temperature gradient, the ones that drive lubricant deformation are the surface tension gradient (thermocapillary shear stress) and evaporation. Evaporation affects the lubricant distortion by removing lubricant and forming a depletion trough.

Thermocapillary shear stress pulls lubricant from areas of hot (low surface tension) to cold (high surface tension), thereby driving lubricant to flow outward from the thermal spot center forming a trough and side ridges. The low viscosity at the thermal spot center enhances the thermocapillary shear flow by increasing lubricant mobility. As shown in Figure 5, without the inclusion of viscosity temperature dependence, there is no significant lubricant distortion. The thickness dependence of viscosity, that is increased viscosity due to stronger intermolecular forces as the film gets thinner, mitigates the amount of lubricant pulled away from the thermal spot center for thinner lubricant systems.

4.2 Disjoining Pressure Study

Disjoining pressure can affect the lubricant in two ways according to the model we have developed. The disjoining pressure value affects evaporation (Equation 9). The disjoining pressure gradient drives lubricant flow from areas of high to low pressure (Equation 14). Because disjoining pressure is a function of lubricant thickness only,

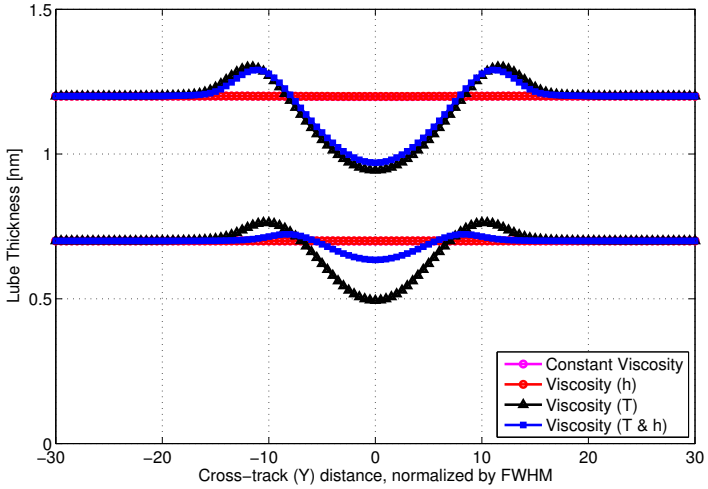

Figure 5: Thermocapillary shear stress, with assistance from thermoviscosity, is a main contributor to lubricant flow under HAMR writing conditions. Evaporation is set to zero in these simulations. If the temperature dependence of viscosity is included (denoted (T) in the legend), a significant amount of lubricant is drawn from the thermal spot center to side ridges in the cooler, higher viscosity regions. The thickness dependence of viscosity (denoted (h) in the legend) mitigates the amount of lubricant pulled away from the thermal spot center for thinner lubricant systems.

the product of the disjoining pressure derivative and the lubricant-air interface gradient determine the direction of this pressure gradient:

$$\nabla\Pi = \frac{d\Pi}{dh}\nabla h$$

The disjoining pressure varies substantially with lubricant thickness, so we consider four thicknesses: 0.5 nm, 0.7 nm, 1.2 nm, and 1.4 nm. These four lubricant systems are subjected to 2 ns of illumination of a 20 nm FHWM thermal spot scanning at a velocity $u_D = 5$ m/s. The maximum center temperature is 350°C . The lubricant has a molecular weight of 2 kg/mol (Zdol 2000). Four cases at each lubricant thickness are considered: (1) no disjoining pressure ($\Pi = 0$), (2) the dispersive component ($\Pi = \Pi^d$), (3) the polar component ($\Pi = \Pi^p$), and (4) the total disjoining pressure ($\Pi = \Pi^d + \Pi^p$). In a head-disk interface system with close physical spacings of less than 2 nm, every Angstrom counts so lubricant deformation on the order of an Angstrom is significant.

4.2.1 Disjoining Pressure Effect on Evaporation

In the first set of simulations, we include all effects (thermocapillary shear stress, thermoviscosity with thickness dependence, Laplace pressure, and thin film evaporation)

for different components of disjoining pressure. The value of disjoining pressure can enhance or inhibit evaporation through its effect on vapor pressure.

The cross-track lubricant and accompanying disjoining pressure profiles at time $t_f = 2$ ns for the case when evaporation is included are shown in Figure 6. All lubricant profiles exhibit a center trough at the maximum temperature location ($y = 0$); this depletion zone is created by mass removal through evaporation and outward mass flow due to thermocapillary shear stress. The side ridges are due to the thermocapillary shear stress. The inclusion of one or both components of disjoining pressure results in a smaller maximum trough depth for all lubricant thicknesses compared with cases excluding disjoining pressure. Disjoining pressure suppresses lubricant removal and flow compared with a bulk film, though the degree of this mitigation depends on lubricant thickness.

The suppression effect of disjoining pressure on lubricant deformation can be explained by analyzing the direction of the thermocapillary shear stress and disjoining pressure gradient. Thermocapillary shear stress always drives lubricant away from the thermal spot center. For Zdol lubricant systems thinner than 1.5 nm, the total disjoining pressure derivative is negative. With the formation of a trough due to evaporation and flow initiated by thermocapillary shear stress, the ∇h points outward from the thermal spot center. Therefore with the negative sign from $\frac{d\Pi}{dh}$, the disjoining pressure gradient $\nabla\Pi$ points inward toward the thermal spot center, the opposite direction of the thermocapillary shear stress.

The thinner lubricants experience little change due to the thermal spot because of the thin film enhancements to viscosity and suppressed thin film evaporation (Figure 6(a)). The peak-to-peak cross-track profile change is less than 0.22 Å for cases that included disjoining pressure at 0.5 nm lubricant thickness. For comparison, typical bond lengths in organic compounds are approximately 100–150 pm = 1–1.5 Å. So for practical purposes, this simulation result for $h_0 = 0.5$ nm can be interpreted as no lubricant deformation. For the $h_0 = 0.7$ nm lubricant system, slight deformation is predicted, ranging from 1.5 Å peak-to-peak variation for the case considering Π^d only to 0.92 Å for the case including the total disjoining pressure.

For the thicker lubricant systems, the inclusion of the polar component of disjoining pressure results in less lubricant deformation compared with the cases including only the dispersive component or no disjoining pressure (Figure 6(b)). With only dispersive disjoining pressure, the peak-to-peak lubricant deformation is 7.0 Å; this deformation is roughly twice the peak-to-peak deformation when either the polar or total disjoining pressure is considered (3.6 Å). For $h_0 = 1.4$ nm, the deformation is greater but the discrepancy when including the polar component or total disjoining pressure is a little smaller: 8.5 Å peak-to-peak for the dispersive component and 5.6 Å for the polar or total disjoining pressure.

The amount of lubricant removed during 2 ns of thermal spot illumination is plotted in Figure 7. Note that the mass of one Zdol PFPE molecule is $M_w/N_A = 0.32\text{e-}24$ kg. When disjoining pressure is excluded, the amount of evaporative mass loss is relatively constant across the four lubricant thicknesses. Dispersive disjoining pressure significantly mitigates evaporation for thinner lubricant systems but has a small effect in thicker systems. The polar disjoining pressure significantly suppresses evaporation for the thinner lubricants where $\Pi^p > 0$ and enhances evaporation over bulk lubricant

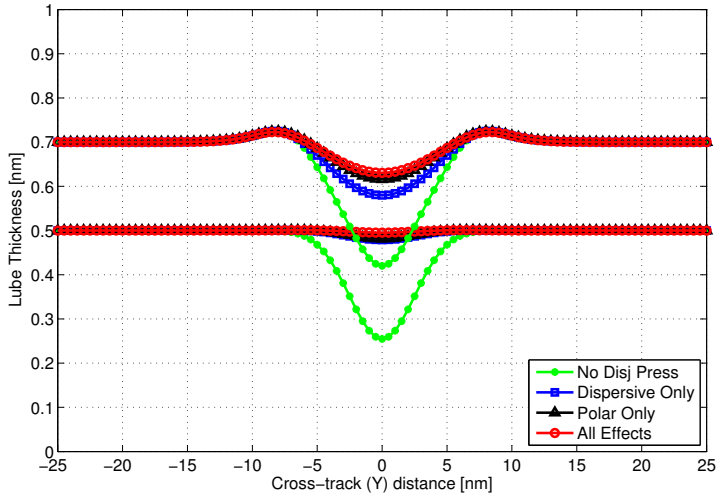

(a) $h_0 = 0.5$ and 0.7 nm

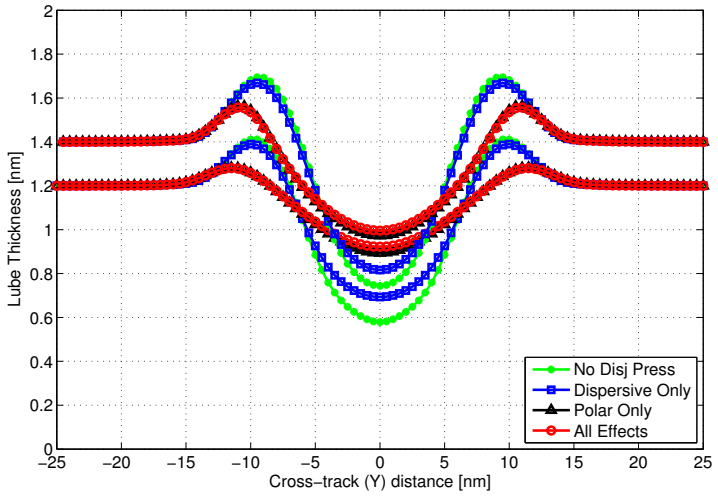

(b) $h_0 = 1.2$ and 1.4 nm

Figure 6: Disjoining pressure study: Cross-track profiles at the center of the depletion trough for lubricant systems of different thicknesses. Thin lubricant systems show little deformation for cases that including disjoining pressure. For thicker films, the inclusion of polar disjoining pressure suppresses lubricant deformation compared with cases without this component. $t_f = 2$ ns, $u_D = 5$ m/s, $T_{max} = 350^{\circ}$C , FWHM = 20 nm.

evaporation for systems thicker than about 1 nm, where $\Pi^p < 0$. When total disjoining pressure is considered for the thinner lubricant systems, the amount of evaporative mass removal is much less than for cases considering the components in isolation. Above 1 nm, where polar disjoining pressure dominates the total disjoining pressure curve and $\Pi < 0$, the amount of mass evaporated for total disjoining pressure follows the polar component curve of evaporation enhancement.

As further illustration of the lubricant properties dictating lubricant deformation, the instantaneous evaporative mass flux and viscosity at 2 ns just before the thermal spot is turned off are plotted in Figures 8 and 9. The evaporation is several orders of magnitude higher at the thermal spot center than at the edges of the domain where the lubricant temperature is close to ambient. The viscosity is much higher for the thinner lubricant systems meaning that it is much harder for the pressure gradients and thermocapillary shear stress to drive lubricant flow.

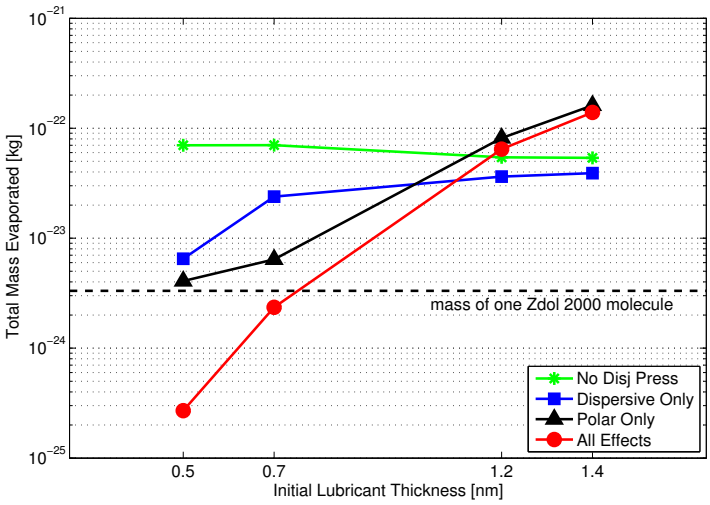

Figure 7: Disjoining pressure study: Amount of mass evaporated after 2 ns of illumination by the laser with a scanning speed $u_D = 5$ m/s. The variation in disjoining pressure with lubricant thickness determines the evaporation rate.

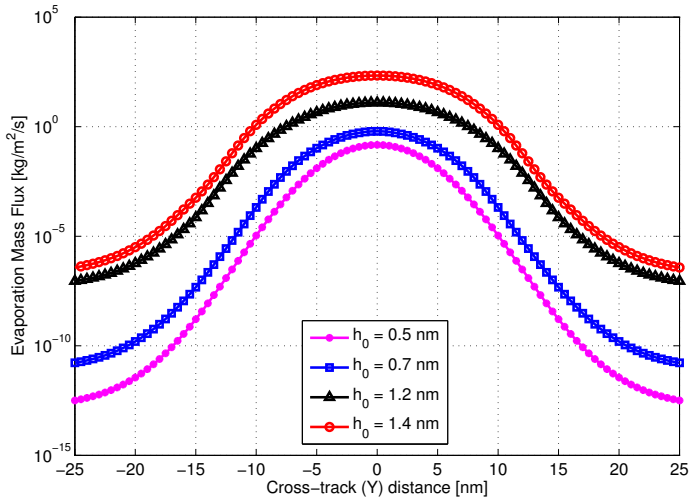

Figure 8: Disjoining pressure study: Instantaneous evaporative mass flux at 2 ns for the cases considering total disjoining pressure $\Pi = \Pi^d + \Pi^p$. Thinner lubricants have orders of magnitude lower evaporation rates compared with thicker lubricants.

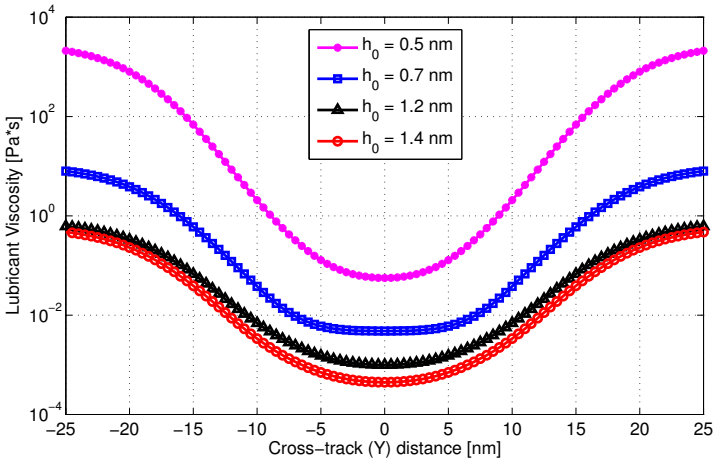

Figure 9: Disjoining pressure study: Instantaneous lubricant viscosity at 2 ns for the cases considering total disjoining pressure $\Pi = \Pi^d + \Pi^p$. Thinner lubricants have orders of magnitude higher viscosity compared with thicker lubricants.

The final Laplace pressure profiles for the simulations that include all effects are plotted for the four lubricant thicknesses in Figure 10. All lubricant systems are subjected to the same temperature profile and hence the same surface tension profile $\gamma(T)$. So the Laplace pressure $\gamma\nabla^2 h$ plotted in Figure 10 is a comparison of the interface mean curvatures ($\kappa = \nabla^2 h/2$). The magnitude and gradient of curvature increase with lubricant thickness, implying that the Laplace pressure contribution to lubricant flow is stronger in the thicker lubricant systems. However, we shall see in an order of magnitude analysis that the amount of lubricant flow driven by the Laplace pressure and disjoining pressure gradients is smaller than the amount driven by thermocapillary shear stress for this system.

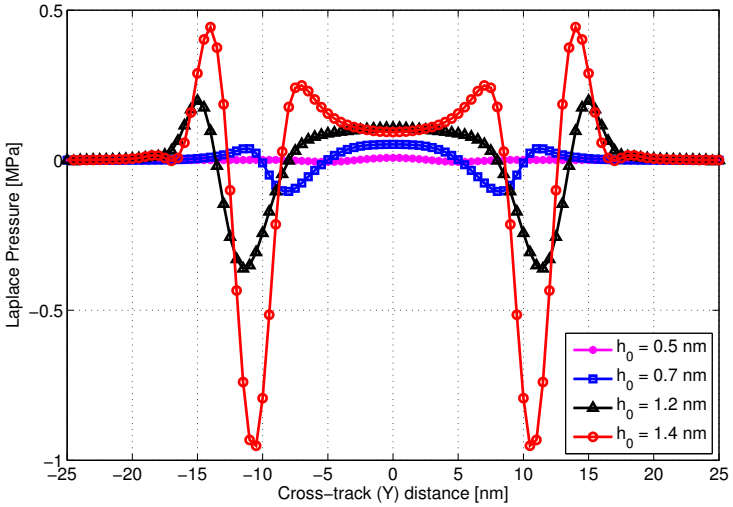

Figure 10: Disjoining pressure study: Final Laplace pressure for the cases considering total disjoining pressure $\Pi = \Pi^d + \Pi^p$. Laplace pressure and hence interface curvature become more severe as the lubricant thickens.

4.2.2 Disjoining Pressure Gradient Effect on Lubricant Flow

In order to isolate the disjoining pressure gradient $\nabla\Pi$ effect on lubricant flow, we suppress the evaporation. We point out that in regimes where $\frac{d\Pi}{dh} > 0$, the lubricant film can become unsteady [24, 30] so that the film spontaneously thickens and thins to form droplets. We repeat the simulations presented above but with evaporation set to zero. The resulting lubricant profiles at 2 ns are plotted in Figure 11 for the four lubricant thicknesses.

For the thin lubricant systems, there is no significant difference between the disjoining pressure cases and the amount of deformation is very small (Figure 11(a)). For $h_0 = 0.5$ nm, the maximum peak-to-peak lubricant thickness difference is only 0.045

Å = 4.5 pm, a value much smaller than typical bond lengths in organic compounds. So for practical purposes, this simulation result is interpreted as no lubricant deformation. The polar component of the disjoining pressure derivative is positive and is therefore in the unstable regime (see Figure 3(b) for $h = 0.5$ nm), but the high viscosity keeps the lubricant from becoming unstable. The $h_0 = 0.7$ nm system shows more lubricant deformation with a maximum peak-to-peak thickness change of approximately 0.9 Å for all cases and a similar trough minimum within 0.2 Å between the four cases. An analysis presented below shows that thermocapillary shear stress is the dominant flow force at $h_0 = 0.7$ nm, so the differences in disjoining pressure derivative across the four cases does not significantly impact the final lubricant profile.

The thicker lubricant systems show significantly more lubricant deformation, on the order of a few Angstroms (Figures 11(b)). Including the polar disjoining pressure component mitigates lubricant flow away from the thermal spot center. For lubricant thicknesses greater than 1 nm, Π^p dominates the Π profile (Figure 3), so it is expected that the lubricant profile for total disjoining pressure will closely match that for cases including only the polar component. The peak-to-peak thickness changes are 3.2 Å for $h_0 = 1.2$ nm and 5.3 Å for $h_0 = 1.4$ nm, which is very close to the peak-to-peak values for the cases when evaporation was considered (3.6 Å and 5.6 Å, respectively). Eliminating evaporation still resulted in significant lubricant deformation, and we will show next that this is due to thermocapillary shear stress.

4.3 Relative Strengths of Lubricant Flow Driving Effects

To compare the relative strengths of the forces driving lubricant flow (not evaporation), we calculate the terms in the governing equation at their characteristic values for each lubricant system. The characteristic lubricant thickness is the initial thickness h_0 and the characteristic temperature gradient is the maximum temperature change $\Delta T = T_{max} - T_0 = 325°\text{C}$ divided by the thermal spot FWHM $L = 20$ nm. The derivative of disjoining pressure is evaluate at the initial thickness:

$$\Pi_0' = \left.\frac{d\Pi}{dh}\right|_{h_0}$$

The spatial derivatives of lubricant thickness and Laplace pressure are taken to be the peak-to-peak profile change divided by the distance over which that change occurs Δx, essentially a linear approximation of major cross-track profile features from Figures 6 and 10. The characteristic flow forces are taken from inside the divergence term of the governing evolution equation:

$$\text{Thermocapillary shear stress:} \qquad F_\gamma = \frac{h_0^2}{2\eta_0}\frac{d\gamma}{dT}\frac{\Delta T}{L}$$

$$\text{Disjoining pressure:} \qquad F_\Pi = \frac{h_0^3}{3\eta_0}\Pi_0'\frac{\Delta h}{\Delta x}$$

$$\text{Laplace pressure:} \qquad F_{Lap} = \frac{h_0^3}{3\eta_0}\frac{\Delta p_{Lap}}{\Delta x}$$

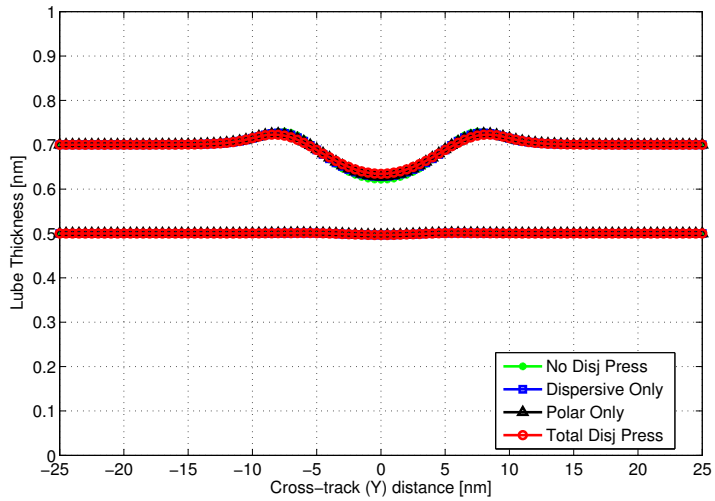

(a) $h_0 = 0.5$ and 0.7 nm

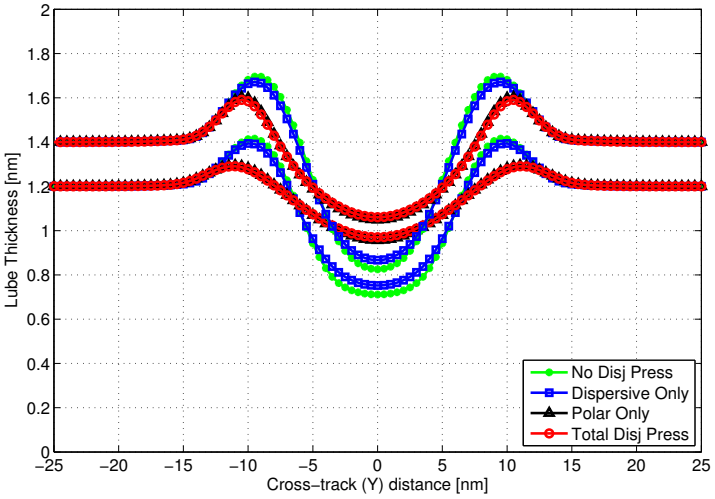

(b) $h_0 = 1.2$ and 1.4 nm

Figure 11: Disjoining pressure study with no evaporation: Cross-track profiles at the center of the depletion trough for lubricant systems of different thicknesses with evaporation suppressed. Total disjoining pressure suppresses lubricant flow away from the thermal spot center for thicker lubricants but has little effect for thin lubricant system. $t_f = 2$ ns, $u_D = 5$ m/s, $T_{max} = 350^{\circ}$C , FWHM = 20 nm.

Table 1 presents the ratio of the thermocapillary shear characteristic flow force F_γ to the other flow forces, flow driven by the disjoining pressure gradient F_Π and the Laplace pressure gradient F_{Lap}. All entries in Table 1 are greater than one, meaning that at these characteristic values the thermocapillary shear stress is responsible for most of the lubricant flow. For thin lubricant systems, F_{Lap} is several orders of magnitude smaller than F_γ and F_Π, so it can be neglected for very thin films. For the thicker lubricant films, all flow forces are of the same order of magnitude with the thermocapillary shear stress driven flow 1–5 times the value of the pressure gradient driven flows.

Table 1: Comparison of characteristic forces driving lubricant flow for different lubricant thicknesses. $\Delta T = 325°\mathrm{C}$, thermal spot size FWHM 20 nm. Thermocapillary shear stress is the dominant flow force for thin lubricant thicknesses and the major flow force in thicker lubricant systems.

h_0	F_γ/F_Π	F_γ/F_{Lap}
0.5 nm	48.0	719
0.7 nm	3.20	29.4
1.2 nm	1.21	5.09
1.4 nm	2.29	1.75

4.4 Thin Film Viscosity Study

The addition of the thin film effect on viscosity is a new contribution of this report. Previous HAMR lubricant simulations based on continuum theory have included only the temperature dependence of viscosity. We conducted simulations at each thickness for two cases: (1) ignoring the thickness dependence of viscosity $\eta_\infty(T)$ and (2) including the temperature and thin film effects on viscosity $\eta(T,h)$ (Equation 6).

The thin film viscosity effect is more important in thinner lubricant films than thicker films (Figure 12). The thinner lubricants show little deformation (< 1 Å peak-to-peak) if the thickness dependence on viscosity is included, while ignoring this dependence results in significant lubricant distortion (peak-to-peak variations of 2.7 Å for $h_0 = 0.5$ nm and 5.3 Å for $h_0 = 0.7$ nm). In contrast, including viscosity thin film effects for thicker lubricants does not appreciably change the predicted lubricant deformation. In Figure 12(b), the lubricants profiles for the two viscosity cases lie practically on top of each other for both lubricant thicknesses. These thin film viscosity results can be explained by examining the viscosity at the final lubricant profiles for all cases, plotted in Figure 13. The thin film viscosity of the thicker lubricants is in close proximity to and of the same order of magnitude as the temperature-only dependent viscosity. However, the thinner lubricant systems the thin film viscosity is several orders of magnitude higher than the temperature-only model. The high viscosity translates to high resistance to flow and therefore little lubricant deformation.

Thus the thin film enhancement of viscosity is important to include in simulations for lubricants less than about 1 nm thick; otherwise, ignoring viscosity's dependence on film thickness will result in unrealistically large lubricant deformation.

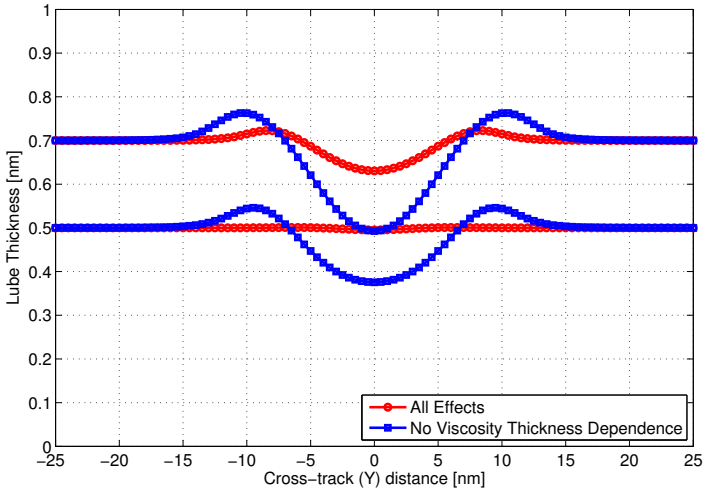

(a) $h_0 = 0.5$ and 0.7 nm

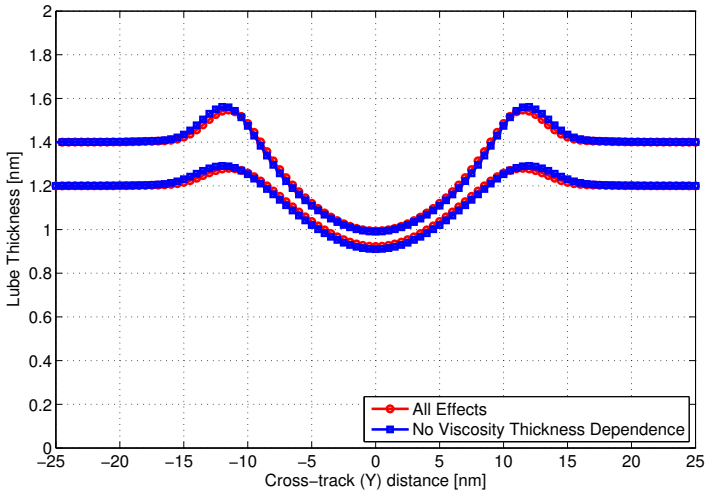

(b) $h_0 = 1.2$ and 1.4 nm

Figure 12: Thin film viscosity study: Cross-track profiles of viscosity at the center of the depletion trough for lubricant systems of different thicknesses. Thin film viscosity is important to consider for thinner lubricants, but it has a smaller effect on lubricant flow for thicker lubricants. $t_f = 2$ ns, $u_D = 5$ m/s, $T_{max} = 350^{\circ}$C , FWHM = 20 nm.

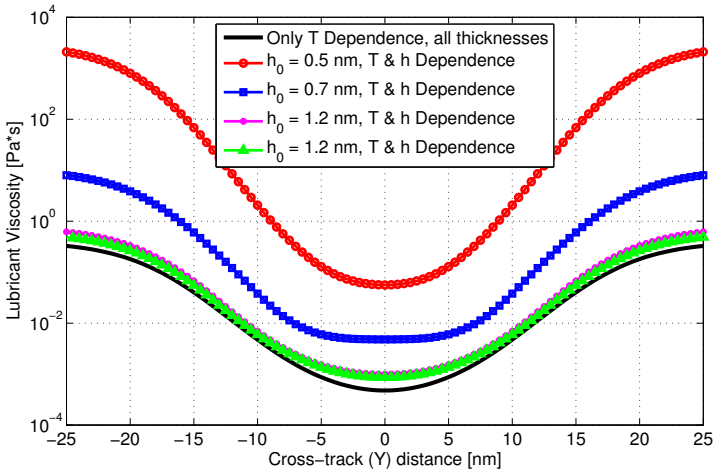

Figure 13: Thin film viscosity study: Viscosity at final lubricant profiles with and without thickness dependence of viscosity. For thick films, neglecting thickness dependence results in similar viscosity values. For thin film, neglecting the thickness dependence of viscosity predicts a value several orders of magnitude lower than the thin film viscosity model. $t_f = 2$ ns, $u_D = 5$ m/s, $T_{max} = 350^{\circ}$C , FWHM = 20 nm.

4.5 Thermal Spot Size Study

Numerous challenges still need to be overcome before a target thermal spot FWHM of 25 nm is reached. In the mean time, larger thermal spots will be generated on the HAMR disk in the design process. The same conditions employed in the previous study are used for prescribed temperature distributions of larger spot sizes than those simulated in Section 4.2 and 4.4. Four film thicknesses are subjected to a thermal spot maximum temperature of 350°C for four thermal spot sizes: FWHM of (1) 1 μm, (2) 100 nm, (3) 50 nm, and (4) 20 nm. The ambient temperature is 25°C , and all lubricant properties and thin film effects are considered. The aim is to determine if the characteristics of the lubricant profiles change with larger thermal spot sizes when attaining the same maximum temperature on the disk.

To directly compare the lubricant profiles, we normalize the cross-track coordinate by the thermal spot FWHM. For both the large and small thermal spots, the deformations of the thin lubricant systems are quite small with essentially no deformation for $h_0 = 0.5$ nm (Figure 14(a)). For $h_0 = 0.7$ nm, the smallest 20 nm FWHM thermal spot resulted in a noticeable trough and side ridges while the larger thermal spots caused smaller deformation, with the largest 1 μm FWHM spot causing a negligible lubricant distortion and no side ridges. The thicker lubricant systems show more lubricant deformation for all thermal spot sizes (Figure 14(b)). The smaller thermal spots cause a trough and side ridges with several Angstroms of peak-to-peak lubricant change. As the thermal spot becomes smaller, the side ridge height increases and the side ridge

peak moves further away from the thermal spot center in the FWHM normalized coordinates. The largest spot again causes only a trough and no side ridges. It is interesting to note how quickly the thermal spot becomes large enough to have negligible sides ridges, indicating a weaker thermocapillary shear stress: the 100 nm FWHM thermal spot lubricant profiles closely resemble the large 1 μm FWHM profiles, not the 20 nm FWHM profiles even though the thermal spot sizes are closer. The governing equation (Equation 14) is highly nonlinear and contains coupled terms, leading to this surprisingly sharp thermocapillary shear stress trend with thermal spot size in the FWHM range 20–100 nm.

The implication of a larger spot to achieve the same peak temperature is a smaller temperature gradient, which means lower thermocapillary shear stress. The ratio of the magnitude of maximum shear stresses $\tau = \frac{d\gamma}{dT}\nabla T$ between to simulations of different thermal spot sizes is equal to the ratio of the characteristic temperature gradients $(T_{max} - T_0)/\text{FWHM}$. Therefore, increasing the thermal spot FWHM by a factor of 50 reduces the thermocapillary shear stress by a factor of 50. The thermocapillary shear stress is too weak in the large spot system to pull lubricant into side ridges, and the resulting trough is mainly due to evaporation. A large thermal spot for the Zdol 2000 simulated in this report appears to be a FWHM greater than 100 nm. In contrast, for smaller thermal spot sizes, thermocapillary shear stress is the main driver of lubricant deformation, pulling lubricant away from the thermal spot center to the side ridges, while evaporation is not as important and deformation is similar whether the evaporation is "on" or "off" (comparing Figure 6(b) to Figure 11(b)).

To directly compare the amount of mass evaporated during the 2 ns of laser illumination, a normalized mass quantity needs to be determined. The total mass evaporated m_{evap} is an integral of the evaporative mass flux over space and time, which is a discretized sum over all control volumes and times steps in our numerical simulation. Because area contributes to the total mass evaporated, we can scale m_{evap} by a characteristic area, thereby to normalizing to thermal spot size. Any measure of area we determine for our axisymmetric Gaussian temperature profile will be proportional to the square of the FWHM, L^2, so we will use this quantity to normalize m_{evap}. Define the normalized evaporated mass as

$$\overline{m}_{evap} \equiv \frac{m_{evap}}{L^2} \tag{15}$$

The values of $\overline{m}_{evap}$ for all cases are listed in Table 2. For all thicknesses, the thermal spot sizes have comparable $\overline{m}_{evap}$ values, usually the same order of magnitude. The larger thermal spot size has the highest $\overline{m}_{evap}$ for all thicknesses except for 1.2 nm, and the smallest thermal spot has the smallest $\overline{m}_{evap}$ for all thicknesses except for 0.7 nm. For the intermediate thermal spot sizes, the 50 nm FWHM spot usually has more normalized evaporation than the larger 100 nm FWHM spot except for 1.4 nm thickness. These non-monotonic trends in amount of normalized evaporated mass are another reflection of the nonlinear governing equation with coupled terms and interesting Zdol lubricant depletion results in the FWHM range 20–100 nm.

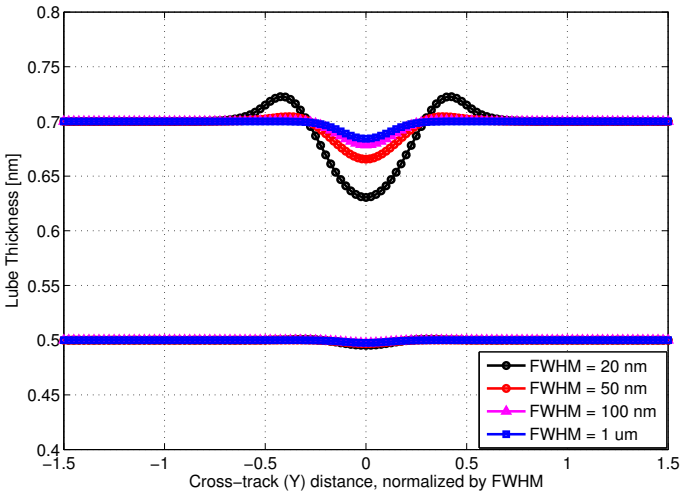

(a) $h_0 = 0.5$ and 0.7 nm

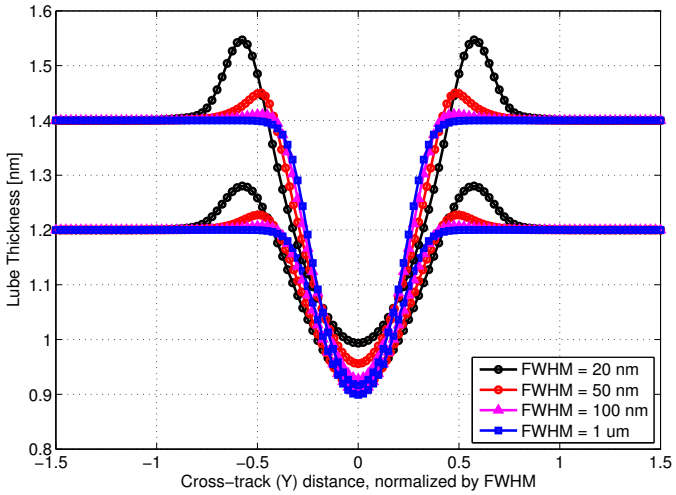

(b) $h_0 = 1.2$ and 1.4 nm

Figure 14: Thermal spot size study: Cross-track profiles at the center of the depletion trough for lubricant systems of different thicknesses and thermal spot sizes. The cross-track coordinate is normalized by the thermal spot FWHM. The small spot profiles have side ridges due to thermocapillary shear stress while the largest spot profiles show no side ridges, only a trough due to evaporation. $t_f = 2$ ns, $u_D = 5$ m/s, $T_{max} = 350^{\circ}$C.

Table 2: Normalized total evaporated mass $\overline{m}_{evap}$ (kg/m^2) for four thermal spot sizes. The amount of normalized evaporated mass is comparable between the all thermal spot sizes, but there are no strictly monotonic trends.

Spot Size	0.5 nm	0.7 nm	1.2 nm	1.4 nm
20 nm FWHM	6.74e-10	5.88e-9	1.61e-7	3.48e-7
50 nm FWHM	9.98e-10	8.20e-9	5.16e-6	4.74e-7
100 nm FWHM	6.79e-10	5.20e-9	2.65e-7	5.30e-7
1 μm FWHM	1.35e-9	7.16e-9	5.78e-7	1.24e-6

4.6 Maximum Temperature Study

Up to this point, all simulations have used a prescribed Gaussian temperature profile that achieves a maximum temperature of 350°C. In effect, we have kept the laser power of the HAMR system constant. In this study, we investigate how lubricant deformation changes with maximum disk temperature, a consequence of varying laser power, for a fixed initial lubricant thickness. For the 1.2 nm lubricant system, we illuminate with a 20 nm FWHM thermal spot with a scanning speed of $u_D = 5$ m/s for $t_f = 2$ ns. The maximum temperature of the thermal spot is varied: $T_{max} =$ 30°C, 150°C, 300°C, 450°C, and 600°C.

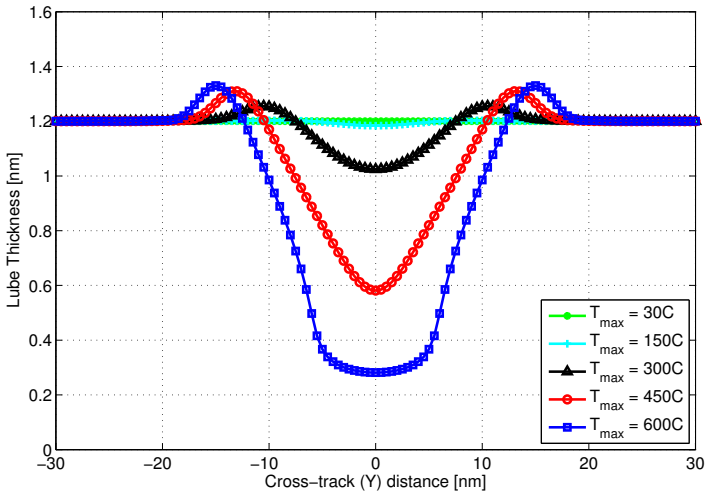

Figure 15: Maximum temperature study: Comparison of lubricant cross-track profiles for different thermal spot maximum temperatures. The lubricant depletion zone width and depth increase with increasing thermal spot maximum temperature. FWHM = 20 nm, $h_0 = 1.2$ nm, $u_D = 5$ m/s.

A higher maximum temperature for a fixed thermal spot size increases the temperature gradient and has two effects: (1) the evaporation rate is higher and (2) the temperature gradient increases, resulting in a stronger thermocapillary shear stress. As shown in Figure 15, as T_{max} increases, the trough becomes wider and deeper and the side ridges grow. No significant lubricant deformation is predicted below 150°C. The bottom of trough in the $T_{max} = 600$°C simulation is flat, indicating that for this lubricant model and peak temperature, the lubricant is not easily thinned below 0.3 nm. The resistance to lubricant flow (thin film viscosity) and evaporation (thin film evaporation) is too high.

If we ignore chemical decomposition and thermal degradation of the molecule, we stipulate that only complete Zdol molecules can evaporate from the thin film. According to Figure 16, no Zdol 2000 molecules are evaporated for T_{max} below approximately 300°C. What little deformation is present at these low temperatures is due to thermocapillary shear stress.

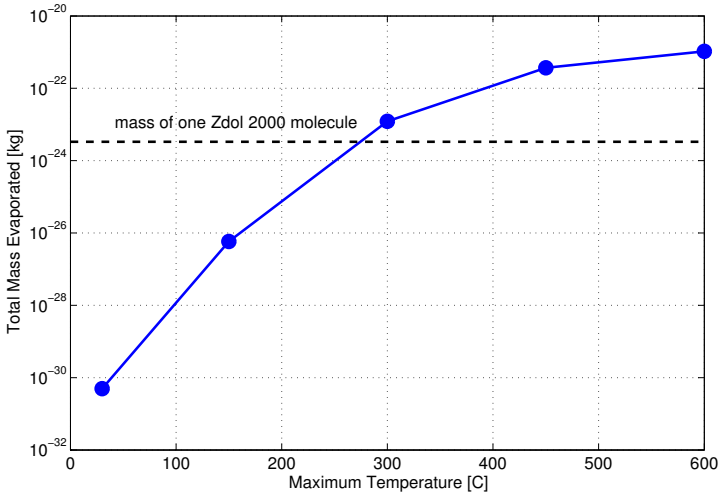

Figure 16: Maximum temperature study: Comparison of total mass evaporated in 2 ns of thermal spot illumination time for different thermal spot maximum temperatures. The mass of one molecule of Zdol 2000 (M_w/N_A) is indicated by the horizontal dashed line. If thermal decomposition is ignored, significant mass loss due to evaporation does not occur below ~ 300°C. FWHM = 20 nm, $h_0 = 1.2$ nm, $u_D = 5$ m/s, $t_f = 2$ ns.

5 Discussion

The simulation conditions of this report—one pass of a FWHM 20 nm thermal spot for an illumination time of 2 ns—are impossible to directly compare with HAMR lu-

bricant experiments in the literature. The resolution of instruments used to measure lubricant thickness change is on the order of microns, experiments often include more than one laser pass, and thickness measurements are taken minutes after the laser illumination, not *in situ*. However, qualitative comparisons can be made, and insights into the published experiment results can be made from our simulation results.

Tagawa et al. [10] illuminated different lubricants of thicknesses larger than 2 nm with a 5 mW laser ($T_{max} \approx 100^{\circ}$C [12]) for a single disk revolution and 60 revolutions; for the 60 revolution cases they observed a raised ridge on the outer diameter side of the track, but no raised ridges for the one revolution cases. Tagawa et al. claimed the laser spot size on the disk surface was 900 nm in diameter, an ambiguous definition. Conservatively we can say the FWHM of this laser spot on the disk is 400 nm. Based on our results in Section 4.5, a small temperature rise less than 100°C above ambient and a large thermal spot with a FWHM of several hundred nanometers will generate a negligible thermocapillary shear stress and the observed deformation is mainly due to evaporation. The raised ridge at the outer diameter edge of the depletion track in [10] could be due to air shearing stresses, as the authors conjectured, or possibly centripetal acceleration effects due to the disk rotation, effects we did not include in our simulations. These effects may have relatively long time scales and only be visible after tens of disk revolutions. Reference [13] presents a plot of lubricant depletion depth after one disk revolution versus laser power for Zdol 2000 systems of 2.12 nm and 0.99 nm thicknesses. The laser spot diameter was again reported to be 900 nm in diameter. For the 0.99 nm thick Zdol 2000, depletion depth at 20 mW ($T_{max} \approx 350^{\circ}$C [12]) is approximately 1.25 Å, between our predicted trough depths for the 1 μm FWHM spot and $T_{max} = 350^{\circ}$C (Figure 14): 0.16 Å trough depth for $h_0 = 0.7$ nm and 3.04 Å for $h_0 = 1.2$ nm.

Several experimental results from the Digital Storage Institute show raised ridges on both sides of the depletion track with the outer diameter edge usually higher [15, 16, 17]. In these experiments, the laser scanned on the disk surface in the radial direction from the inner to outer diameter to create a 10–20 μm depletion track visible by an optical surface analyzer. The outer edge of the depletion track may see more accumulation because the laser is scanning from the inner to the outer radius, creating a leading edge accumulation zone similar to roller processes, as well as air shearing stress and centripetal acceleration.

Qualitatively, our simulation results show similar trends as other simulation studies of Zdol-type lubricants under HAMR conditions. These trends include lubricant depletion zone width and depth increase with disk surface temperature, side ridges forming due to thermocapillary shear stress, and thickness dependence of the severity of lubricant depletion [18, 19, 21, 20].

The simulations by Wu [18, 19] show more lubricant deformation due to evaporation and a smaller thermocapillary shear stress effect than we predict for similar simulation conditions. We share the same governing evolution equation, but this equation incorporates models for lubricant properties of viscosity, evaporation, disjoining pressure, and surface tension. Even when we suppress the polar component and use similar conditions ($h_0 = 1.45$ nm, FWHM = 80 nm, $\Delta T = 265^{\circ}$C , $t_f = 20$ ns), the plots in [18] show a deeper trough ($h_0 - h_{min} \approx 1.06$ nm) than we predict ($h_0 - h_{min} = 0.142$ nm). Additionally, our simulations predict notable thermocapillary shear stress side ridges,

while plots in [18] show no side ridges. Our evaporation models are different than the model given in [18, 19], which predicts a higher evaporation rate according to our comparison simulations. Other researchers replicated Wu's lubricant depletion model and found that this model over-predicts evaporation compared with Tagawa's experiments [42]. In [18], evaporation is suppressed to isolate thermocapillary shear stress, similar to Figure 5 in this report. We conducted similar simulations with only dispersive disjoining pressure and no evaporation. While we predict 0.98 Å peak-to-peak distortion in the down-track profile, Figure 5(b) in [18] shows approximately 0.16 Å peak-to-peak deformation. Our viscosity model must decrease faster with temperature than the one employed in [18, 19], where the general form of the viscosity model is provided but not the values of the coefficients.

Matsuoka et al. [21] predicted significant lubricant deformation for $h_0 = 2$ nm at relatively mild thermal conditions; the maximum temperature increase was only 50°C or 100°C and the Gaussian thermal spot had a standard deviation of 1 μm, corresponding to a FWHM of 2.355 μm. While we cannot replicate simulations from [21] because our disjoining pressure model is only valid up to 2 nm, we can comment on the reason for significant deformation for relatively mild thermal conditions. Possibly the 2 nm lubricant system is too thick for the dispersive interaction effects on disjoining pressure and their surface tension model to retard lubricant flow as demonstrated in our simulations for thicknesses 1.4 nm and below (Figure 6). At a lubricant thickness of 2 nm, the dispersive component of disjoining pressure, the only component considered in [21], is already quite small (Figure 3(a)).

This continuum mechanics model is only as good as the incorporated lubricant property models, most notably the disjoining pressure and viscosity. It is possible that surface tension γ_{LV} isn't a viable quantity when the system consists of one or two monolayers. Maybe there should be one quantity to represent the enhanced intermolecular forces. Marchon and Saito have approached this concept with the temperature dependent Hamaker constant [25].

In this report, we have not considered thermal decomposition or the polydispersity. Experiments suggest thermal decomposition of Zdol consists of cleavage of the fluorinated ether backbone [6], meaning the disk could be covered with severed Zdol molecules having only one functional end-group after the writing process. Lubricant properties such as viscosity and disjoining pressure would change due to the different nature of the polymer molecules. More experimental study of thermal decomposition processes and kinetics of the leading contender for the HAMR lubricant is needed, and these results could be incorporated into an improved continuum model to predict HAMR lubricant behavior. Lubricants on hard drives are not pure materials, but rather a mixture of different molecular weight components. Because evaporation is strongly dependent on molecular weight, the degree of polydispersity will determine how the evaporation rate changes with time as the lighter molecules evaporate first [48, 22].

We have shown significant lubricant deformation under HAMR writing for high thermal gradient, high temperature simulations. How the lubricant will recover after the thermal spot has passed is the subject of an upcoming report.

6 Conclusion

We have developed a continuum model to predict HAMR lubricant behavior on the disk under write conditions. For the first time, the effects of functionalized end-groups on disjoining pressure and thin film viscosity have been considered. Under an applied thermal spot, lubricant deformation is driven by the surface tension gradient (thermocapillary shear stress) and evaporation. The low viscosity at the thermal spot center enhances the thermocapillary shear flow by increasing lubricant mobility. Total disjoining pressure suppresses lubricant removal and flow compared with models that consider only the van der Waals force contribution to disjoining pressure, though the degree of this mitigation depends on lubricant thickness. Above 1 nm thickness, evaporation is enhanced over the bulk value for the particular disjoining pressure model for Zdol used in this report because disjoining pressure is negative. Thinner lubricants less than 1 nm have orders of magnitude lower evaporation rates and higher viscosities compared with thicker lubricants which means lubricant depletion is harder to achieve for very thin films if the lubricant does not thermally decompose. For simulations of lubricants less than about 1 nm thick, ignoring viscosity's dependence on film thickness will result in unrealistically large lubricant deformation. A larger thermal spot size above 100 nm FWHM generates a lower thermocapillary shear stress that becomes be too weak to pull lubricant into side ridges, and the resulting trough is mainly due to evaporation. This is in contrast to the smaller thermal spots with the higher temperature gradient: thermocapillary shear stress is the main driver of lubricant deformation, pulling lubricant away from the thermal spot center to the side ridges, while evaporation is not as important and deformation is similar whether the evaporation is considered or not. No significant lubricant deformation is predicted below 150°C for a 2 ns thermal spot illumination time. As the thermal spot maximum temperature increases, the lubricant depletion zone depth and width increase. This report is a first step to simulate functional lubricants under HAMR write conditions. Future improvements to the model include consideration of viscoelastic, thermal decomposition, and polydispersity effects.

Acknowledgements

This work was supported by the Computer Mechanics Laboratory at University of California, Berkeley, Mechanical Engineering Department. The authors would also like to thank the Information Storage Industry Consortium (INSIC) Extremely High Density Recording (EHDR) program and the International Disk Drive Equipment and Materials Association (IDEMA) Advanced Storage Technology Consortium (ASTC) for providing early funding for this research.

References

[1] R. Rottmayer, S. Batra, D. Buechel, W. Challener, J. Hohlfeld, Y. Kubota, L. Li, B. Lu, C. Mihalcea, K. Mountfield, K. Pelhos, C. Peng, T. Rausch, M. Seigler,

D. Weller, and X. Yang, "Heat-Assisted Magnetic Recording," *IEEE Transactions on Magnetics*, vol. 42, no. 10, pp. 2417–2421, 2006.

[2] M. Kryder, E. Gage, T. McDaniel, W. Challener, R. Rottmayer, G. Ju, Y.-T. Hsia, and M. Erden, "Heat Assisted Magnetic Recording," *Proceedings of the IEEE*, vol. 96, no. 11, pp. 1810–1835, 2008.

[3] "International Technical Roadmap: Magnetic Data Storage - the technology of magnetic hard disk drives (HDDs)," IDEMA Advanced Storage Technology Committee (ASTC), Tech. Rep., January 2013.

[4] A. Q. Wu, Y. Kubota, T. Klemmer, T. Rausch, C. Peng, Y. Peng, D. Karns, X. Zhu, Y. Ding, E. K. Chang, Y. Zhao, H. Zhou, K. Gao, J.-U. Thiele, M. Seigler, G. Ju, and E. Gage, "HAMR Areal Density Demonstration of 1+ Tbpsi on Spinstand," in *The Magnetic Recording Conference (TMRC) 2012*, San Jose, CA, USA, 2012.

[5] N. Shukla, A. J. Gellman, and J. Gui, "The Interaction of CF 3CH 2OH and (CF 3CF 2) 2O with Amorphous Carbon Films," *Langmuir*, vol. 16, no. 16, pp. 6562–6568, 2000.

[6] R. Lei, A. Gellman, and P. Jones, "Thermal stability of Fomblin Z and Fomblin Zdol thin films on amorphous hydrogenated carbon," *Tribology Letters*, vol. 11, no. 1, pp. 1–5, 2001.

[7] L. Li, P. Jones, and Y.-T. Hsia, "Effect of chemical structure and molecular weight on high-temperature stability of some Fomblin Z-type lubricants," *Tribology Letters*, vol. 16, no. 1-2, pp. 21–27, 2004.

[8] G. W. Tyndall and R. J. Waltman, "Thermodynamics of confined perfluoropolyether films on amorphous carbon surfaces determined from the time-dependent evaporation kinetics," *The Journal of Physical Chemistry B*, vol. 104, no. 30, pp. 7085–7095, 2000.

[9] M. Stirniman, S. Falcone, and B. Marchon, "Volatility of perfluoropolyether lubricants measured by thermogravimetric analysis," *Tribology Letters*, vol. 6, pp. 199–205, 1999.

[10] N. Tagawa, R. Kakitani, H. Tani, N. Iketani, and I. Nakano, "Study of Lubricant Depletion Induced by Laser Heating in Thermally Assisted Magnetic Recording System–Effect of Lubricant Film Materials," *IEEE Transactions on Magnetics*, vol. 45, no. 2, pp. 877–882, 2009.

[11] N. Tagawa, H. Andoh, and H. Tani, "Study on Lubricant Depletion Induced by Laser Heating in Thermally Assisted Magnetic Recording Systems: Effect of Lubricant Thickness and Bonding Ratio," *Tribology Letters*, vol. 37, pp. 411–418, 2010.

[12] N. Tagawa and H. Tani, "Lubricant Depletion Characteristics Induced by Rapid Laser Heating in Thermally Assisted Magnetic Recording," *IEEE Transactions on Magnetics*, vol. 47, no. 1, pp. 105–110, 2011.

[13] N. Tagawa, T. Miki, and H. Tani, "Depletion of monolayer liquid lubricant films induced by high-frequency pulsed-laser heating in thermally assisted magnetic recording," *Microsystem Technologies*, vol. 18, no. 9-10, pp. 1353–1357, 2012.

[14] Y. Ma, L. Gonzaga, C. An, and B. Liu, "Effect of Laser Heating Duration on Lubricant Depletion in Heat Assisted Magnetic Recording," *IEEE Transactions on Magnetics*, vol. 47, no. 10, pp. 3445–3448, 2011.

[15] Y. Ma, X. Y. Chen, J. M. Zhao, S. K. Yu, B. Liu, H. L. Seet, K. K. Ng, J. F. Hu, and J. Z. Shi, "Experimental Study of Lubricant Depletion in Heat Assisted Magnetic Recording," *IEEE Transactions on Magnetics*, vol. 48, no. 5, pp. 1813–1818, 2012.

[16] Y. Ma, X. Chen, and B. Liu, "Experimental Study of Lubricant Depletion in Heat Assisted Magnetic Recording over the Lifetime of the Drive," *Tribology Letters*, vol. 47, no. 2, pp. 175–182, 2012.

[17] ——, "Experimental study of lubricant depletion in heat assisted magnetic recording: effects of laser heating duration and temperature," *Microsystem Technologies*, vol. 19, no. 2, pp. 291–297, 2013.

[18] L. Wu, "Modelling and simulation of the lubricant depletion process induced by laser heating in heat-assisted magnetic recording system," *Nanotechnology*, vol. 18, p. 215702, 2007.

[19] L. Wu and F. E. Talke, "Modeling laser induced lubricant depletion in heat-assisted-magnetic recording systems using a multiple-layered disk structure," *Microsystem Technologies*, vol. 17, no. 5-7, pp. 1109–1114, 2011.

[20] Y. Zeng, W. Zhou, X. Huang, and S. Yu, "Numerical study on thermal-induced lubricant depletion in laser heat-assisted magnetic recording systems," *International Journal of Heat and Mass Transfer*, vol. 55, no. 4, pp. 886–896, 2012.

[21] H. Matsuoka, K. Oka, Y. Yamashita, F. Saeki, and S. Fukui, "Deformation characteristics of ultra-thin liquid film considering temperature and film thickness dependence of surface tension," *Microsystem Technologies*, vol. 17, no. 5-7, pp. 983–990, 2011.

[22] W. Zhou, Y. Zeng, B. Liu, S. Yu, W. Hua, and X. Huang, "Evaporation of Polydisperse Perfluoropolyether Lubricants in Heat-Assisted Magnetic Recording," *Applied Physics Express*, vol. 4, p. 095201, 2011.

[23] M. Scarpulla, C. Mate, and M. Carter, "Air shear driven flow of thin perfluoropolyether polymer films," *Journal of Chemical Physics*, vol. 118, no. 7, pp. 3368–3375, 2003.

[24] T. Karis, "Lubricants for the Disk Drive Industry," in *Lubricant Additives: Chemistry and Applications*, L. Rudnick, Ed. CRC Press, 2009, ch. 22, pp. 523–584.

[25] B. Marchon and Y. Saito, "Lubricant Thermodiffusion in Heat Assisted Magnetic Recording," *IEEE Transactions on Magnetics*, vol. 48, no. 11, pp. 4471–4474, 2012.

[26] A. Oron, S. Davis, and S. Bankoff, "Long-scale evolution of thin liquid films," *Reviews of Modern Physics*, vol. 69, no. 3, pp. 931–980, 1997.

[27] A. W. Adamson, *Physical Chemistry of Surfaces*, 5th ed. John Wiley & Sons, Inc., 1990.

[28] P.-G. de Gennes, F. Brochard-Wyart, and D. Quere, *Capillarity and Wetting Phenomena: Drops, Bubbles, Pearls, Waves*. Springer Science+Business Media, Inc., 2004.

[29] S. Morris, "Surface Energy and Its Manifestations," University of California, Berkeley, ME 268 Lecture, Fall 2011.

[30] B. V. Derjaguin, N. Churaev, and V. Muller, *Surface Forces*. New York: Consultants Bureau, Plenum Publishing Corporation, 1987.

[31] C. M. Mate, "Taking a Fresh Look at Disjoining Pressure of Lubricants at Slider-Disk Interfaces," *IEEE Transactions on Magnetics*, vol. 47, no. 1, pp. 124–130, 2011.

[32] T. Karis and G. Tyndall, "Calculation of spreading profiles for molecularly-thin films from surface energy gradients," *Journal of Non-Newtonian Fluid Mechanics*, vol. 82, pp. 287–302, 1999.

[33] Y.-T. Hsia, P. Jones, and L. R. White, "Can Contact-Angle Measurements Determine the Disjoining Pressure in Liquid Nanofilms on Rigid Substrates?" *Langmuir*, vol. 20, no. 23, pp. 10 073–10 079, 2004.

[34] G. W. Tyndall, P. Leezenberg, R. J. Waltman, and J. Castenada, "Interfacial interactions of perfluoropolyether lubricants with magnetic recording media," *Tribology Letters*, vol. 4, no. 2, pp. 103–108, 1998.

[35] G. W. Tyndall, R. J. Waltman, and D. Pocker, "Concerning the interactions between Zdol perfluoropolyether lubricant and an amorphous-nitrogenated carbon surface," *Langmuir*, vol. 14, pp. 7527–7536, 1998.

[36] R. J. Waltman, D. Pocker, and G. W. Tyndall, "Studies on the interactions between ZDOL perfluoropolyether lubricant and the carbon overcoat of rigid magnetic media," *Tribology Letters*, vol. 4, pp. 267–275, 1998.

[37] R. Powell, W. Roseveare, and H. Eyring, "Diffusion, thermal conductivity, and viscous flow of liquids," *Industrial & Engineering Chemistry*, vol. 33, no. 4, pp. 430–435, 1941.

[38] T. Karis, B. Marchon, V. Flores, and M. Scarpulla, "Lubricant spin-off from magnetic recording disks," *Tribology Letters*, vol. 11, no. 3-4, pp. 151–159, 2001.

[39] J. H. Poynting, "V. Change of state: Solid-liquid," *Philosophical Magazine Series 5*, vol. 12, no. 72, pp. 32–48, 1881.

[40] V. P. Carey, *Liquid-Vapor Phase-Change Phenomena*, 2nd ed. Taylor & Francis Group, LLC, 2008.

[41] G. M. Rosenblatt, "Evaporation from Solids," in *Treatise on Solid State Chemistry*, N. Hannay, Ed. New York: Plenum Press, 1976, vol. 6A, ch. 3, pp. 165–240.

[42] W. Zhou, Y. Zeng, B. Liu, S. Yu, and X. Huang, "A Model for Laser Induced Lubricant Depletion in Heat-Assisted Magnetic Recording," *Tribology Letters*, vol. 45, pp. 411–416, 2012.

[43] M. S. Mayeed and T. Kato, "Density Variation in the Ultrathin Liquid Perfluoropolyether Films on Solid Surfaces," *Tribology Transactions*, vol. 44, no. 3, pp. 444–450, 2001.

[44] H. Kubotera and D. Bogy, "Numerical simulation of molecularly thin lubricant film flow due to the air bearing slider in hard disk drives," *Microsyst Technol*, vol. 13, no. 8-10, pp. 859–865, 2007.

[45] S. Patankar, *Numerical Heat Transfer and Fluid Flow*. Hemisphere Publishing Corporation, 1980.

[46] T. Yabe, T. Aoki, G. Sakaguchi, and P. Wang, "The compact CIP (Cubic-Interpolated Pseudo-particle) method as a general hyperbolic solver," *Computers & Fluids*, 1991.

[47] T. Aoki, "Multi-dimensional advection of CIP (Cubic-Interpolated Propagation) scheme," *Computational Fluid Dynamics Journal*, vol. 4, no. 3, pp. 279–291, 1995.

[48] M. Stirniman and J. Gui, "Polydispersity Effects in the Evaporation of Perfluoropolyether Thin Films," *Journal of Physical Chemistry B*, vol. 106, no. 23, pp. 5967–5971, 2002.